

Impact-sliding wear response of 2.25Cr1Mo steel tubes: Experimental and semi-analytical method

Meigui YIN^{1,2}, Thibaut CHAISE², Liwen WANG^{3,*}, Daniel NÉLIAS², Minhao ZHU¹, Zhenbing CAI^{1,*}

¹ Tribology Research Institute, Key Lab of Advanced Technologies of Materials, Southwest Jiaotong University, Chengdu 610031, China

² Univ Lyon, INSA Lyon, CNRS, LaMCoS, UMR5259, Villeurbanne 69621, France

³ Research Institute of Dongfang Electric Corporation, Chengdu 611731, China

Received: 4 March 2020 / Revised: 4 December 2020 / Accepted: 29 June 2021

© The author(s) 2021.

Abstract: The impact-sliding wear behavior of steam generator tubes in nuclear power plants is complex owing to the dynamic nature of the mechanical response and self-induced tribological changes. In this study, the effects of impact and sliding velocity on the impact-sliding wear behavior of a 2.25Cr1Mo steel tube are investigated experimentally and numerically. In the experimental study, a wear test rig that can measure changes in the impact and friction forces as well as the compressive displacement over different wear cycles, both in real time, is designed. A semi-analytical model based on the Archard wear law and Hertz contact theory is used to predict wear. The results indicate that the impact dynamic effect by the impact velocity is more significant than that of the sliding velocity, and that both velocities affect the friction force and wear degree. The experimental results for the wear depth evolution agree well with the corresponding simulation predictions.

Keywords: impact-sliding wear; semi-analytical; 2.25Cr1Mo steel tube; nuclear reactors

1 Introduction

In 1957, the world's first commercial nuclear power plant (Shipping Port, USA) began generating electricity, indicating that humans had entered the era of peaceful nuclear energy usage [1]. Currently, second- and third-generation nuclear power reactors are operated normally worldwide. In the early 21st century, to improve the thermal efficiency and operational safety of existing nuclear power reactors, researchers began to study and develop fourth-generation nuclear reactors, whose commercial operations are expected to begin after the 2030s [2, 3].

The steam generator tube is an important component of nuclear power plants that operate under harsh operating conditions. Currently, Inconel 600, 690, and 800 steam generator tubes are installed in most active nuclear power plants [4, 5]. The 2.25Cr1Mo steel tube has been widely used in fourth-generation

sodium-cooled experimental fast reactors, primarily owing to its high resistance to hydrogen attacks and excellent high-temperature strength [6]. However, owing to the combined effects of high flow rate, high fluid pressure and temperature, and narrow clearance between tubes and anti-vibration bars, various wear behaviors were observed on their surfaces, which significantly degraded their operating performance and service life [7–9].

The wear types that have been investigated for this type of tube include sliding, impact, and impact-sliding wear. These wear types are classified primarily based on the relative movements of the interacting surfaces. In sliding wear, one wear surface undergoes tangential slip motion relative to the other surface. Hence, the motion model of the test rigs used to investigate this type of wear always involves a fixed sample and another friction pair performing a reciprocating slip motion. Numerous specific conditions,

* Corresponding authors: Liwen WANG, E-mail: 243550101@qq.com; Zhenbing CAI, E-mail: caizb@swjtu.cn

Nomenclature			
n	Impact-sliding wear cycles	$F_s(t)$	Friction force vs. time (N)
Δh_{\max}	Maximum wear depth for n cycle	$F_{s\max}$	Maximum friction force (N)
h_n	Maximum wear depth after n wear cycles (μm)	a	Half-width of contact area (mm)
Δn	Increment of wear cycles	b	Half-length of contact area (mm)
$h_{\Delta n}$	Increment of wear depth after Δn wear cycles (μm)	Δs	Displacement amplitude per wear cycle (μm)
V	Wear volume (μm^3)	G	Shear modulus of tube (MPa)
$F_i(t)$	Impact force vs. time (N)	$\bar{\mu}$	Average friction coefficient
m	Mass of impact block (g)	j	Collected data point
$\delta_i(t)$	Impact displacement vs. time (μm)	μ_j	Friction coefficient for each data point
E	Effective elastic modulus (MPa)	d_v	Wear volume for each cycle (μm^3)
R	Effective radius (mm)	w_c	Wear coefficient ($\mu\text{m}^3/(\text{N}\cdot\text{m})$)
R_1	Diameter of cylinder (mm)	d_s	Increment of sliding amplitude (μm)
R_2	Outer diameter of tube (mm)	ΔE	Friction dissipated energy per cycle (mJ)
E_1	Young's modulus of cylinder (MPa)	v_s	Sliding velocity (mm/s)
E_2	Young's modulus of tube (MPa)	v_s	Sliding velocity vs. time (mm/s)
ν_1	Poisson's ratio of cylinder	E_d	Cumulated dissipated energy (mJ)
ν_2	Poisson's ratio of tube	$p(x,y)$	Contact pressure of point (x,y) (Pa)
v_0	Initial impact velocity (mm/s)	p_{\max}	Maximum compressive pressure (Pa)
δ_{\max}	Maximum impact displacement (μm)	d_h	Increment of wear depth per cycle (μm)
F_{\max}	Maximum impact force (N)	d_A	Increment of wear area per cycle (μm^2)
t_c	Phase of compression (ms)	$d_{h\max}$	Increment of wear depth at point of maximum contact pressure (μm)
$v_i(t)$	Impact velocity vs. time (mm/s)	Δt	Increment of wear contact time (ms)
μ	Friction coefficient	A	Contact area per cycle (mm^2)

such as temperature, liquid solution, and contact model, have been investigated for these wear types [10–13]. Impact wear occurs when the steam generator tube is continuously impacted by another component. Souillard et al. [14, 15] used shakers to create an impact between a tube and a plate; the impact force or frequency during the wear process was adjustable. Cai et al. [16–18] controlled the kinetic impact energy to conduct impact wear testing on various steam-generating tubes. The dynamic responses of the impact force and energy dissipation can be monitored in real time during the wear process. In impact-sliding wear, normal impact and tangential slip movements occur simultaneously between the tube and its wear

pair during the wear process. Guo et al. [19] and Van Herpen et al. [20] used a vibration generator to excite the tube and investigated its impact-sliding wear behavior. Chen [21] employed two voice coil motors with an orthogonal layout to drive the tube and its wear pair separately. The load and frequency of the impact motion, as well as the frequency and displacement amplitude of the sliding motion, can be set arbitrarily. Yin et al. [22, 23] developed an impact-sliding wear test rig to investigate the wear behavior of nuclear grade 690 alloy tubes under different impact kinetic energies and sliding velocities. Compared with pure impact or sliding wear, the relative motion between components that experience

impact-sliding wear was various and complex; consequently, relevant experimental studies pertaining to this wear type became more complicated.

The wear behavior of steam generator tubes is a complex dynamic process, and various studies have been conducted to comprehensively analyze the effects of different variables on their wear responses and damage mechanisms. Guo et al. [24] and Mi et al. [25] discovered that during the sliding wear process, as the normal load increased, the wear coefficient first decreased and then remained relatively constant. Xin et al. [26, 27] reported that the friction coefficient and wear volume increased with the sliding amplitude. Guan [28] concluded that increasing the initial impact velocity decreased the energy absorption ratio during each impact wear cycle. Souillart et al. [14, 15] discovered that by increasing the impact angle, the wear volume first increased and then decreased. Sato et al. [29] observed that the wear volume caused by impact-sliding wear was significantly larger than that caused by pure impact or sliding wear under the same impulse. In addition to the various experimental studies conducted to investigate the wear behaviors of various steam generator tubes, different theoretical analyses and numerical calculation models of wear have been implemented. The classical Archard wear law and energy dissipation wear model have been widely employed to predict the wear characteristics of materials. The dynamic mechanical properties can be analyzed using the Hertz contact theory and Coulomb's law [30]. The mechanical response, energy dissipation, wear mechanism, and other physical phenomena associated with impact-sliding wear are extremely complex. However, experimental studies and theoretical analyses remain relatively scarce and under-developed.

In the present study, the effects of various impact and sliding velocities on the impact-sliding wear behavior of a test tube were experimentally and numerically investigated. Several mathematical formulas relevant to the mechanical equations and wear evolution of the test samples were derived based on the Hertz elastic contact theory and Archard wear law. All the test and simulation results were evaluated to obtain a better understanding of the tribological characteristics during the impact-sliding wear process

and to provide reference values for the wear analyses of steam generator tubes.

2 Materials and methods

2.1 Experimental materials

The sample tubes used in this study were 2.25Cr1Mo chromium molybdenum alloy steel, and the cylindrical impact head was a GCr15 bearing steel. A cylinder-tube contact mode was applied in this study (Fig. 1(b)). The diameter and length of the cylinder were 10 and 15 mm, respectively. The tube had an external diameter of 16 mm, thickness of 2.5 mm, and length of 30 mm. The mechanical properties of the investigated materials are listed in Table 1. Because both materials were homogenous, it was assumed that the material properties did not affect the analysis or experimental results. Prior to wear testing, the samples were ground with 1,500 grit paper and polished with 0.5 μm diamond suspension. After processing, all test samples were ultrasonically cleaned in ethyl alcohol and then dried with compressed air.

2.2 Impact-sliding wear test rig

An impact-sliding wear test rig (Fig. 1(a)) was designed to investigate the wear behavior of the test samples. During each wear cycle, the tube (4 in Fig. 1(a)) slid at a constant velocity (v_s) driven by a linear motor along the sliding direction (1 in Fig. 1(a)). The cylinder (9 in Fig. 1(a)) was fixed on the impact block (6 in Fig. 1(a)), and its kinetic energy was provided by a linear motor in the impact direction (7 in Fig. 1(a)). When the velocity of the impact block reached a specified value (v_0), the impact block was disengaged from the motor and rubbed against the sliding tube (4 in Fig. 1(a)). After the impact-sliding wear process was completed, the impact block was reversed (Fig. 1(c)). Additional details regarding to the test rig are available in Refs. [19, 20]. In each wear cycle, the normal impact load and tangential friction force exerting on the test tube over time were acquired using two piezoelectric force sensors (2 and 8 in Fig. 1(a)). The variations in the displacement of the impact block were recorded using a grating sensor (5 in Fig. 1(a)) in the impact direction.

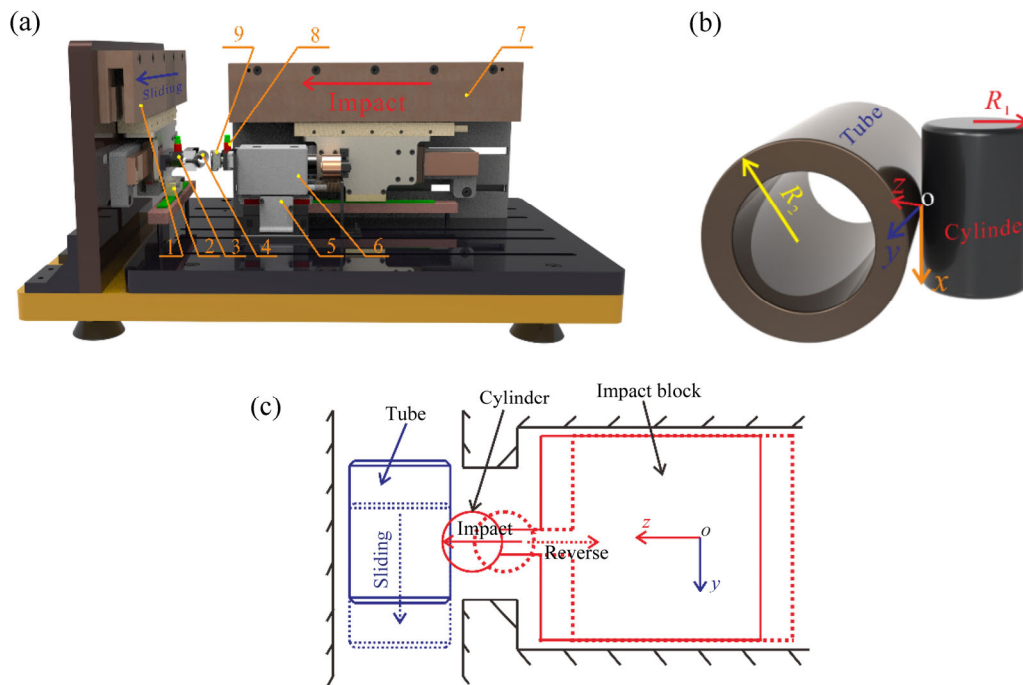


Fig. 1 Schematic illustration of impact-sliding wear. (a) Impact-sliding wear test rig (1-Linear motor-sliding, 2-Sliding displacement sensors, 3-Impact force sensors, 4-Tubes, 5-Grating sensors, 6-Impact blocks, 7-Linear motor impacts, 8-Friction force sensors, and 9-Cylinders), (b) tube and cylinder, and (c) impact-sliding wear process.

Table 1 Mechanical properties of cylinder and tube.

Material	E (GPa)	ν	Density, ρ (kg/m ³)	Shear modulus (GPa)	Hardness (HV _{0.2})
2.25Cr1Mo	179.32	0.33	7.75	67.5	207.02
GCr15	210	0.30	7.81	74.33	763.11

2.3 Semi-analytical method

A semi-analytical contact solver, which enables the solution of discretized three-dimensional (3D) contact problems in an extremely short central processing unit time, was used to predict the wear evolution of the tube under different cycles in each impact-sliding wear test. The Hertzian contact mechanics and Archard wear law were applied to analyze the wear evolution and mechanical behavior; details regarding this semi-analytical element method are available in Refs. [31–33]. Because the impact velocity of the cylinder was significantly lower than that of the elastic waves propagating in the investigated materials, the impact-sliding wear contact behavior was considered to be quasi-static. A flowchart of the iteration procedure used to simulate this wear is shown in Fig. 2. Initial input parameters, including the normal force, sliding displacement, material properties, and geometry, were

required. At each time step, the normal force was determined from the current impact velocity, and the normal impact load was used as the input to the classical elastic–plastic contact model. During the solution process, the contact pressure and wear deformation were simultaneously solved via an iterative

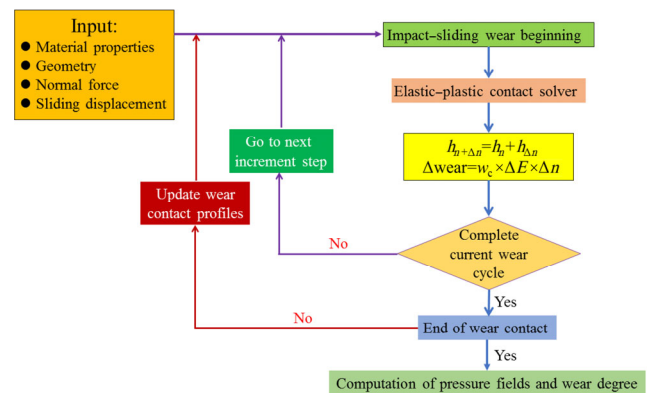


Fig. 2 Flow chart of semi-analytical impact-sliding model.

procedure based on the conjugate gradient method, and the repeated evolution of contact deformation was realized via a fast Fourier transform. Repeated iterations for each load and displacement increment were tested until convergence was achieved [34, 35].

The effects of the impact velocity of the cylinder and sliding speed of the tube on the impact-sliding wear behavior of the tube were investigated in this study. The impact velocity was selected based on the actual range of normal impact force generated between the steam generator tube and its supporter, whereas the sliding velocity was selected based on the actual fretting amplitude. The main experimental parameters of the impact-sliding wear test are listed in Table 2. The wear test for each set of experimental parameters was repeated three times (I, II, and III) to ensure the accuracy and repeatability of the results.

After wear testing, the surface morphologies and profiles of all the wear scars were observed using a scanning electron microscope (JSM-6610, Japan) and a 3D optical microscope (Bruker Contour GT-1, Germany), respectively. All the wear test results were analyzed to comprehensively understand the evolution of the mechanical and tribological mechanisms of the tube under different wear conditions.

3 Results and discussion

3.1 Dynamic mechanical behavior

The test tube was subjected to pure normal impact wear when the sliding speed was zero ($v_s = 0$, Fig. 3). The Hertz theory of normal contact between two

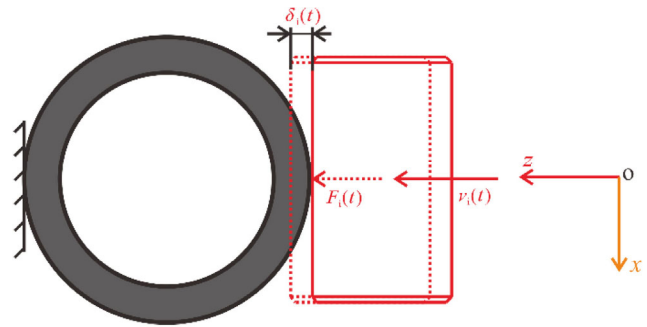


Fig. 3 Schematic illustration of impact wear of tube.

perpendicularly crossed elastic cylinders was used to investigate the mathematical relationships among the impact velocity, force, and displacement. The impact displacement and force were determined from the impact velocities. Based on Newton’s second law and the Hertz elastic theory, at each instant during the impact contact process, the rate of change of the impact velocity depends on the interaction force and compressive displacement, which are expressed in Eqs. (1) and (2). The impact force and compressive displacement reached their maximum values as the instantaneous impact velocity was reduced to zero, which is consistent with Eqs. (3)–(7) [36, 37]. The constant k_0 represents the stiffness parameter, which depends on the structural and functional characteristics of the impact-sliding wear test rig.

$$F_i(t) = -m \frac{d^2 \delta_i(t)}{dt^2} \tag{1}$$

$$F_i(t) = k_0 E \sqrt{R} \delta_i^{\frac{3}{2}}(t) \tag{2}$$

Table 2 Impact-sliding wear test conditions.

Contact model		Cylinder/Tube					
Mass of impact block (g)		600					
Number of wear cycles, n		10 ⁴					
Temperature (°C)		27					
I	Impact velocity (mm/s)	60					
	Sliding velocity (mm/s)	0	30	45	60	75	90
II	Impact velocity (mm/s)	30	45	60	75	90	—
	Sliding velocity (mm/s)	0					
III	Impact velocity (mm/s)	30	45	60	75	90	—
	Sliding velocity (mm/s)	60					

$$\begin{cases} R = \sqrt{R_1 R_2} \\ \frac{1}{E} = \frac{1 - \nu_1^2}{E_1} + \frac{1 - \nu_2^2}{E_2} \end{cases} \quad (3)$$

$$-m \frac{d^2 \delta_i(t)}{dt^2} = k_0 E \sqrt{R} \delta_i^{\frac{3}{2}}(t) \quad (4)$$

$$\left(\frac{d\delta_i(t)}{dt} \right)^2 = v_0^2 - k_0 \frac{4E\sqrt{R}}{5m} \delta_i^{\frac{5}{2}}(t) \quad (5)$$

$$\delta_{i\max} = \left(\frac{5mv_0^2}{4k_0 E \sqrt{R}} \right)^{\frac{2}{5}} \quad (6)$$

$$F_{i\max} = k_0 E \sqrt{R} \delta_{i\max}^{\frac{3}{2}} \quad (7)$$

Based on the experimental results, the approximate value of k_0 was derived to be 0.06. The concrete expressions for the maximum impact displacement and force are expressed in Eqs. (8) and (9), respectively. Figure 4 shows the experimental and calculated data for both the maximum impact displacement and force at different impact velocities. When the impact velocity increased from 30 to 90 mm/s, the maximum impact displacement increased from approximately 15.6 to 37.6 μm , as shown in Fig. 4(a). The corresponding maximum impact forces increased from 43.4 to 161.7 N, as shown in Fig. 4(b). All the data obtained from the derived mathematical equations agreed well with the experimental results.

$$\delta_{i\max} = \left(\frac{5mv_0^2}{0.24E\sqrt{R}} \right)^{\frac{2}{5}} \quad (8)$$

$$F_{i\max} = 0.06E\sqrt{R}\delta_{i\max}^{\frac{3}{2}} \quad (9)$$

The period during which the cylinder impacted the tube can be segregated into an initial compression phase (t_c) and a subsequent restitution phase (t_r). Because we assumed that these phases were perfectly elastic and that kinetic energy dissipation was negligible, the impact deformation was perfectly reversible ($t_c \approx t_r$) [38]. The compression phase was terminated when the velocity of the impact block became zero. At this moment, both the compressive relative displacement and interaction impact force were maximized, as indicated by Eq. (10). Hence, based on Eqs. (4) and (11), as well as the experimental results, the relationship between the compression period t_c and initial impact velocity v_0 is defined as shown in Eq. (12) [36, 38].

$$\begin{cases} \dot{\delta}_i(t_c) = 0 \\ \delta_i(t_c) = \delta_{i\max} \\ F_i(t_c) = F_{i\max} \end{cases} \quad (10)$$

$$\begin{cases} t_c = \int_0^{\delta_{i\max}} \frac{1}{v_i(t)} d\delta_i(t) \\ v_i(t) = \frac{d\delta_i(t)}{dt} = \left(v_0^2 - k_0 \frac{4E\sqrt{R}}{5m} \delta_i^{\frac{5}{2}}(t) \right)^{\frac{1}{2}} \end{cases} \quad (11)$$

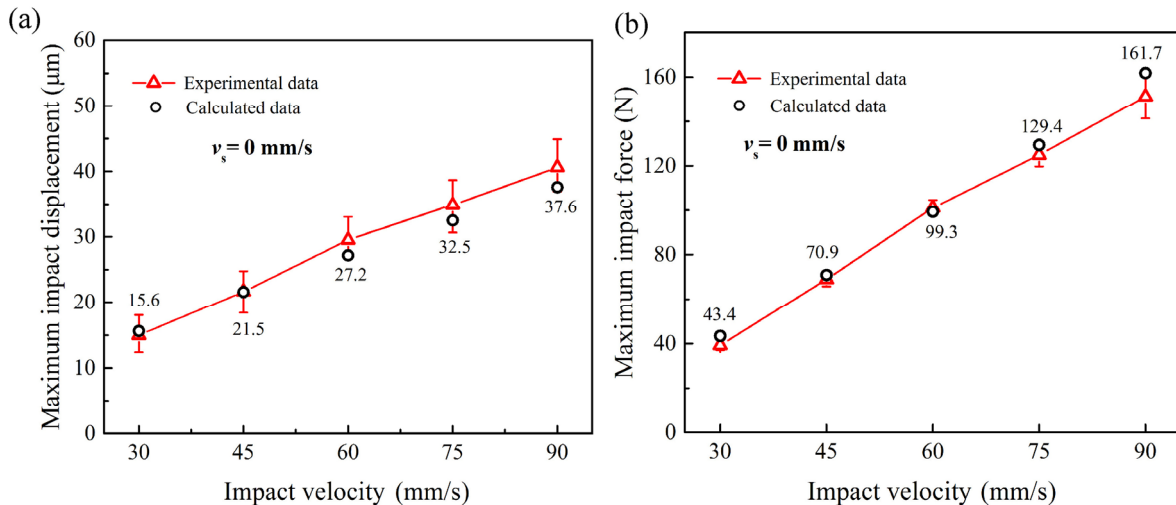


Fig. 4 Maximum impact displacement and force vs. impact velocity: (a) maximum impact displacement and (b) maximum impact force.

$$t_c = 4.89 \left(\frac{m^2}{E^2 R v_0} \right)^{\frac{1}{5}} \tag{12}$$

The variation in the Hertz impact force over time is nonlinear and expressed as a definite integral. Therefore, the expression of the impact force vs. time can be substituted with a sine function to simplify the treatment for Eq. (13) [36–38]. Substituting Eq. (13) into Eq. (2) yields the expression for the impact displacement at any time node, as indicated by Eq. (14):

$$F_i(t) = F_{i\max} \sin\left(\frac{\pi t}{2t_c}\right) \tag{13}$$

$$\begin{aligned} \delta_i(t) &= \left(\frac{F_i(t)}{0.06E\sqrt{R}} \right)^{\frac{2}{3}} \\ &= \left(\frac{F_{i\max}}{0.06E\sqrt{R}} \right)^{\frac{2}{3}} \sin^{\frac{2}{3}}\left(\frac{\pi t}{2t_c}\right), \quad 0 \leq t \leq 2t_c \end{aligned} \tag{14}$$

Figures 5(a) and 5(b) present the evolutions of the impact force and displacement over time at different impact velocities, respectively. The impact force and displacement, which varied with respect to time, were calculated using Eqs. (13) and (14), respectively. As shown in Fig. 5, the results obtained using the present expressions were similar to the experimental data.

In this study, the speed ranges of the moving tube and cylinder were in units of millimeters per second;

hence, the impact-sliding wear can be considered as a quasi-static process. Within each cycle, the shape of the wear contact area between the cylinder and tube remained elliptical. Moreover, because full sliding conditions were used and the two materials indicated similar Young’s moduli and Poisson’s ratios, no coupling occurred between the normal and tangential problems. Hence, it can be inferred that the tangential friction force did not contribute to the normal elastic approach. The normal contact in this study remained within the framework of Hertz’s hypotheses [37, 39].

Figure 6(a) presents the changes in the impact force with respect to time at various sliding velocities and an impact speed of 60 mm/s. The differences between the results for different sliding velocities were insignificant. At a constant sliding velocity of the tube, the evolution of the dynamic impact force in a single wear cycle, which was affected by various impact velocities, is shown in Fig. 6(b). The results indicate that the impact force subjected to the tube during the impact-sliding wear process was identical to that in the case of pure impact wear. The experimental data for the maximum impact force for different numbers of wear cycles under each impact-sliding wear condition are shown in Figs. 6(c) and 6(d). No significant changes were indicated in the maximum impact force as the number of wear cycles increased.

Figure 7(a) presents curves that indicate changes in

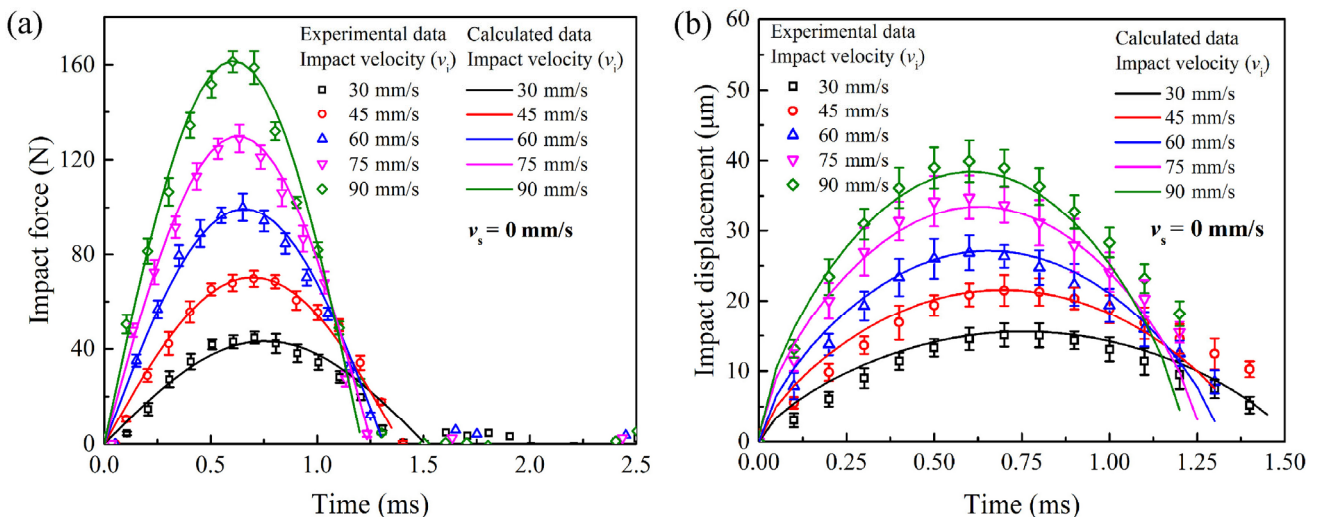


Fig. 5 Impact force and displacement vs. time for various impact velocities: (a) impact force with respect to v_i and (b) impact displacement with respect to v_i .

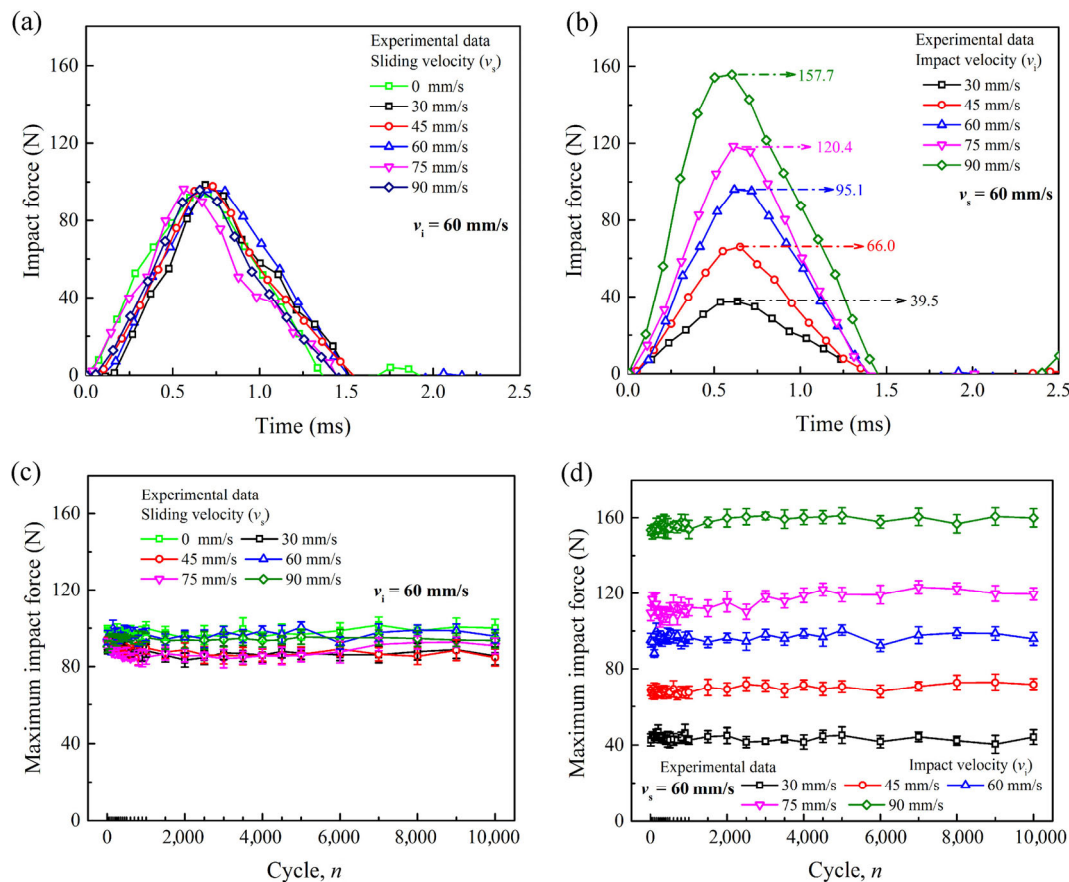


Fig. 6 Impact force for various impact and sliding velocities: (a) impact force for various v_s , $n = 10$; (b) impact force for various v_i , $n = 10$; (c) maximum impact force vs. cycles for various v_s ; (d) maximum impact force vs. cycles for various v_i .

the impact displacement over time at various sliding velocities. Despite the slight difference among them, they were considered the same in the range of experimental errors. Figure 7(b) shows that, when the impact velocity increased from 30 to 90 mm/s, the experimental data corresponding to the maximum impact displacement increased from approximately 15.2 to 38.3 μm . The data agreed well with the calculation results.

The impact displacement was primarily driven by the impact velocity, and the sliding velocity affected the tangential friction force. Although coupling occurred between the normal and tangential behaviors, the impact velocity affected the impact displacement, and it was a second-order effect.

During each cycle of the impact-sliding wear contact process, the tube propagated unidirectionally along the y -axis in a steady sliding motion, as shown in Fig. 8(a). A tangential friction force was exerted along with the normal impact force on the wear surface, as

shown in Fig. 8(b). The normal impact force resulted in Hertz contact stresses with maximal subsurface shear stresses, whereas the tangential friction force resulted in shear tractions. The effects of both stress on wear must be determined [37].

Figures 9(a) and 9(b) show the evolutions of the maximum friction force with respect to the number of wear cycles for different tube sliding velocities and cylinder impact speeds. The data presented were acquired using a piezoelectric force sensor. It is noteworthy that the magnitude of the friction force depends on many factors, such as the normal impact force, surface morphology, and contact time; hence, in many cases, it is difficult to predict a definite value of the friction force based on standard mathematical expressions for different wear conditions [40]. Under each wear condition investigated in this study, the friction forces increased with the number of wear cycles at the initial running-in wear stage, and then fluctuated slightly within a stable range as the wear

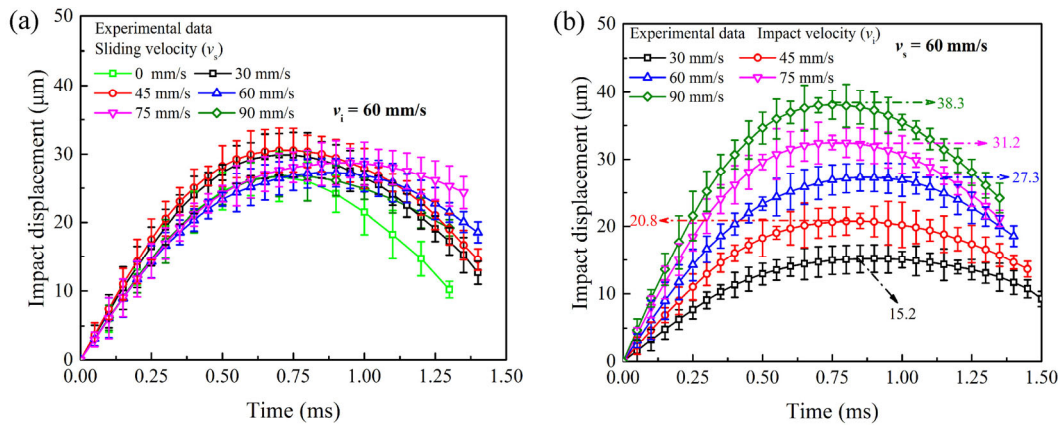


Fig. 7 Impact displacement for various impact and sliding velocities, $n = 10$. (a) Impact displacement for various v_s ; (b) impact displacement for various v_i .

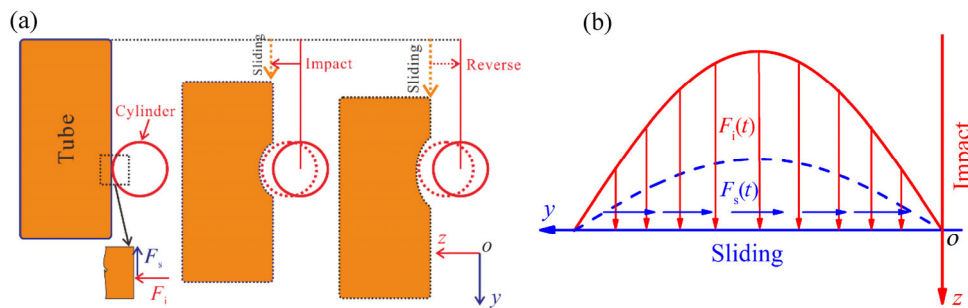


Fig. 8 Diagram of impact-sliding wear process: (a) cylinder wear with tube; (b) impact and friction forces.

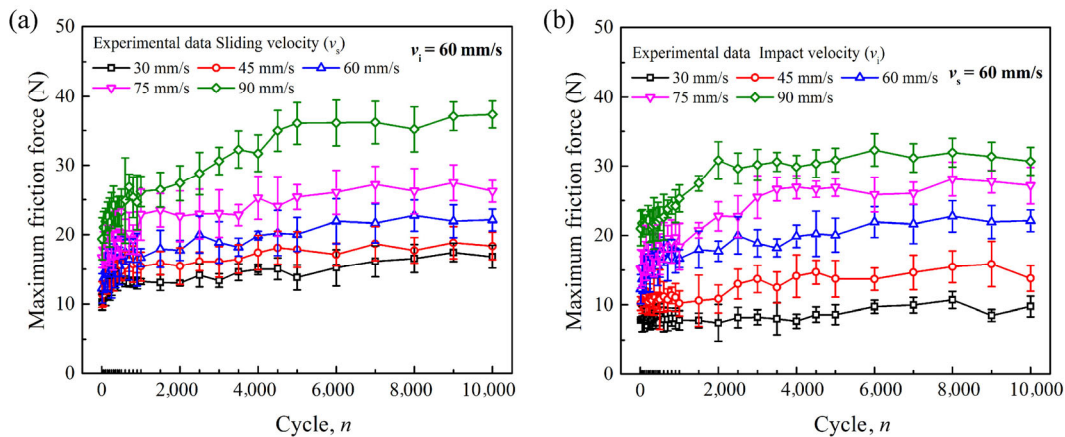


Fig. 9 Friction force vs. number of cycles for different impact and sliding velocities: (a) friction force for different v_s ; (b) friction force for different v_i .

began to stabilize. Additionally, the maximum friction force increased with the tube’s sliding velocity or the cylinder’s impact speed.

3.2 Wear evolution

In the present study, it was assumed that no stick or partial slip occurred between the cylinder and tube during the entire impact-sliding wear process; in

other words, the wear contact surface was in a complete sliding condition. Hence, the friction coefficient provided a crude first-order approximation of the quotient of the tangential frictional force and normal impact force, as expressed by Eq. (15):

$$\mu = \frac{F_s(t)}{F_i(t)} = \frac{F_{smax}}{F_{imax}} \tag{15}$$

During the wear process, the continuous impact between the cylinder and sliding tube along the perpendicular axes (with radii R_1 and R_2 , respectively) resulted in an elliptical contact area. Figure 10 shows the contact area at the moment when the impact speed of the cylinder was reduced to zero. The width and length of the semi-axes of the contact area can be calculated using Eq. (16) [41]. The width and length were affected by the impact velocity; both increased with the impact velocity of the cylinder, as shown in Fig. 11(b).

$$\begin{cases} a \approx \sqrt{R_1 \delta_{\text{imax}}} \\ b \approx \sqrt{R_2 \delta_{\text{imax}}} \end{cases} \quad (16)$$

The magnitude and direction of the tube’s sliding velocity remained constant in each wear cycle; hence, the relative displacement of the wear surface was proportional to the sliding velocity of the tube, as indicated by Eq. (17) [38]. Based on the relationships

$$\Delta s \propto v_s \quad (17)$$

$$\Delta s = \frac{3(2-\nu)\mu F_{\text{imax}}}{16Gb} \quad (18)$$

$$\mu \propto \frac{16Gb}{3(2-\nu)F_{\text{imax}}} \Delta s \quad (19)$$

$$\bar{\mu} = \sum_{j=1}^{30} \frac{\mu_j}{30} \quad (20)$$

among the normal impact force, tangential displacement, and shear stress, the displacement of the surface points inside the wear contact area is expressed in Eq. (18) [38]. It can be concluded that the friction coefficient is always proportional to the surface displacement, and the length of the contact area is inversely proportional to the impact force, as shown in Eq. (19) [38, 41]. Thirty data points were acquired from each impact-sliding wear test. The mean friction coefficient is the average value of all the friction coefficients, as expressed by Eq. (20).

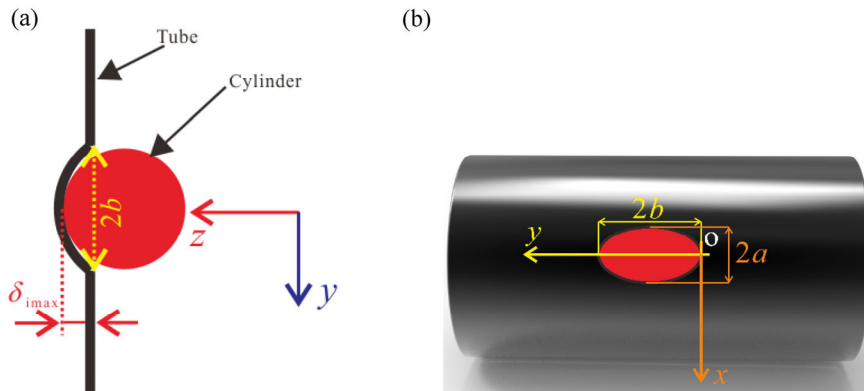


Fig. 10 Illustration of cylinder contact with tube: (a) contact between cylinder and tube; (b) contact area.

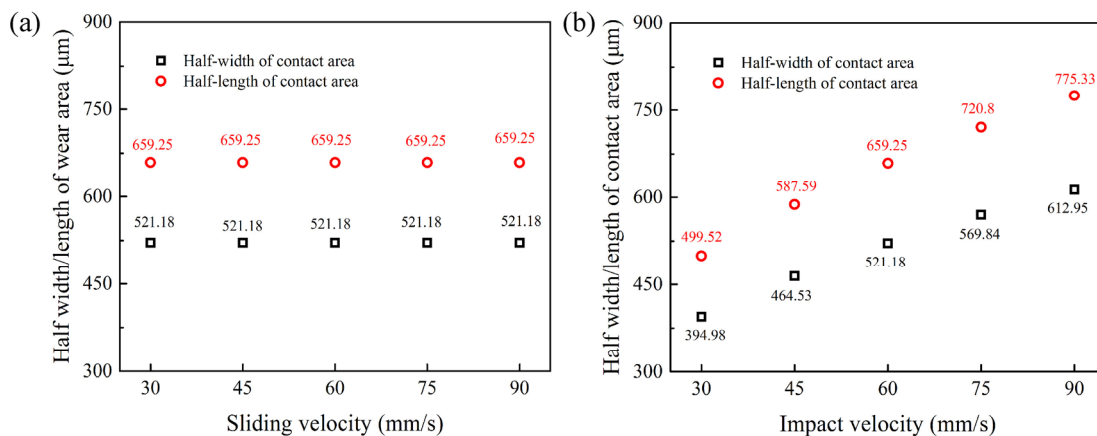


Fig. 11 Half width and length of contact area under different wear conditions: (a) $v_i = 60$ mm/s; (b) $v_s = 60$ mm/s.

Figures 12(a) and 12(b) show the changes in the friction coefficient over the wear cycles under different wear conditions. The variation tendency against number of cycles was similar to that of the friction force. In the running-in stage, the friction coefficient increased continuously with the number of wear cycles, which is attributable to the increased adhesion and abrasion on the wear contact surface. After equilibrium was attained between the generation and ejection of wear debris, the wear process stabilized, and the friction coefficient fluctuated only within a small range. The average friction coefficient for the entire wear process increased from approximately 0.156 to 0.295 as the sliding velocity increased from 30 to 90 mm/s at an impact velocity of 60 mm/s. In this case, the normal impact force remained unchanged, and the tangential friction force increased with the sliding velocity; hence, the average friction coefficient increased, as shown in Fig. 12(c). At a sliding velocity of 60 mm/s, the average friction coefficient decreased from 0.215 to 0.167 as the impact velocity increased from 30 to 90 mm/s. When the sliding velocity was constant, both the tangential friction force and normal impact force increased with the impact velocity.

However, the effects of the impact velocity on the normal impact force were more significant than those on the tangential friction force. Therefore, the friction coefficient decreased slightly as the impact velocity increased, as shown in Fig. 12(d).

Wear is often manifested as material loss due to the relative motion between contacting surfaces. Figure 13 shows the difference in the maximum wear depth and wear volume of the wear scar under various wear conditions. The data presented were obtained using a 3D optical microscope. Both the wear volume and maximum wear depth increased with the sliding or impact velocity. When the impact velocity was 60 mm/s, the maximum wear depth and wear volume increased by approximately 1.4 μm and $6.68 \times 10^5 \mu\text{m}^3$, respectively, as the tube's sliding velocity increased from 30 to 90 mm/s, as shown in Fig. 13(a). As the impact velocity increased from 30 to 90 mm/s at a sliding velocity of 60 mm/s, the maximum wear depth and wear volume increased from approximately 1.03 to 6.49 μm and from 3.38×10^5 to $16.12 \times 10^5 \mu\text{m}^3$, respectively, as shown in Fig. 13(b).

The wear process is a friction energy dissipation process that generates wear particles [42]. The classical

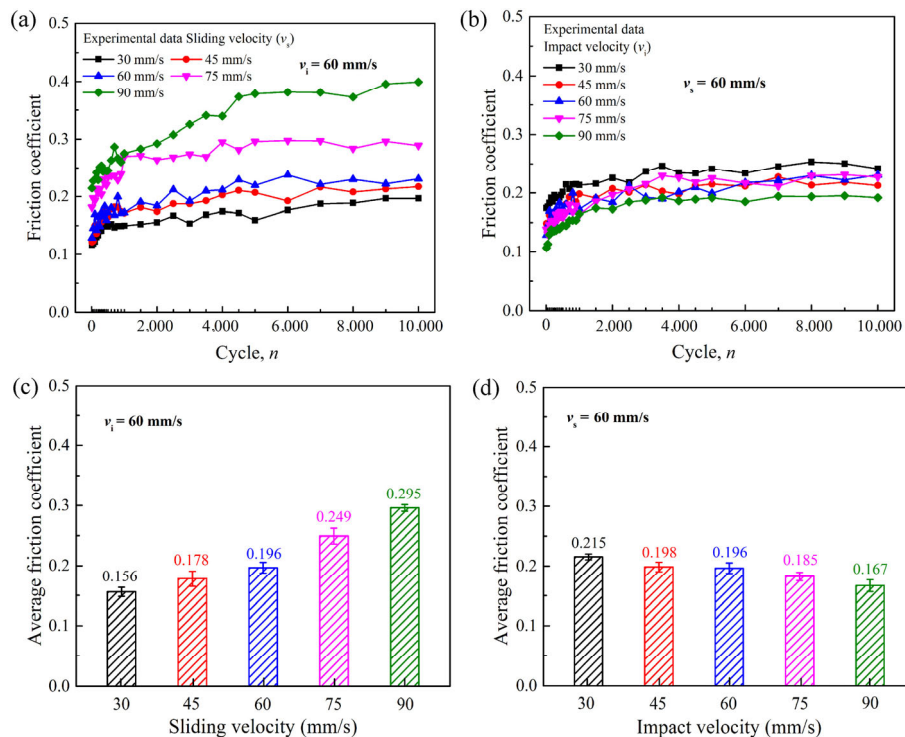


Fig. 12 Friction coefficient for different impact and sliding velocities: (a) friction coefficient for various v_s ; (b) friction coefficient for various v_i ; (c) average friction coefficient vs. v_s ; (d) average friction coefficient vs. v_i .

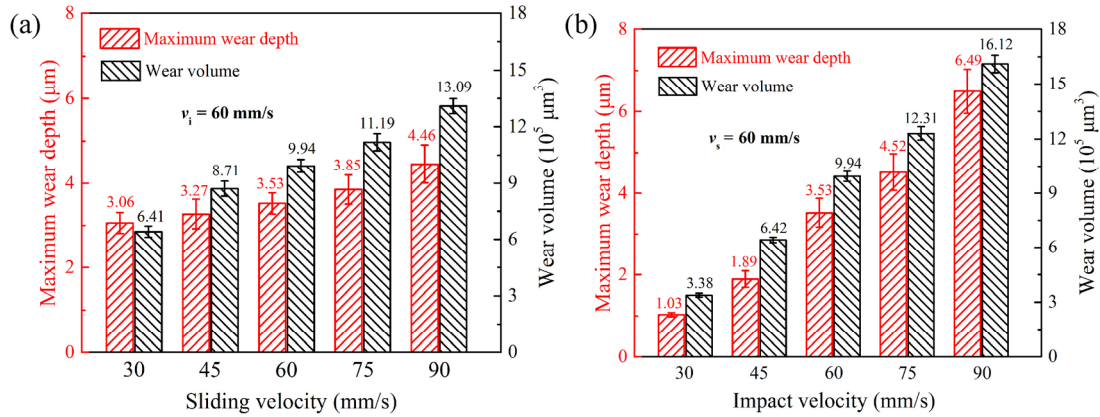


Fig. 13 Wear depth and volume for various impact and sliding velocities, $n = 10^4$. (a) Wear depth and volume for various v_s ; (b) wear depth and volume for various v_i .

Archard model assumes that the wear volume is proportional to the normal load and sliding displacement, and inversely proportional to the material's hardness [43]. Combined with the Coulomb friction model, the Archard model can be transformed into Eq. (21). In this study, the dissipated friction energy in each wear cycle can be calculated using Eq. (22), and the total friction energy dissipated in each wear test is the sum of all the ΔE values, as indicated by Eq. (23). The wear volume appears to be directly proportional to the dissipated friction energy, and the wear coefficient under each wear condition can be calculated using Eq. (24). The values of the total wear volume were obtained from the experimental results.

$$d_v = w_c F_i(t) d_s = w_c \frac{F_s(t)}{\bar{\mu}} d_s \quad (21)$$

$$\Delta E \approx \int_0^{2t_c} \bar{\mu} F_i(t) v_s dt \quad (22)$$

$$E_d \approx \sum_{N=1}^{10^4} \Delta E = 10^4 \Delta E, \quad N = 1 - 10,000 \quad (23)$$

$$\begin{cases} d_v = w_c \int_0^{2t_c} F_i(t) v_s dt = \frac{w_c}{\bar{\mu}} \int_0^{2t_c} F_s(t) v_s dt = \frac{w_c}{\bar{\mu}} \Delta E \\ V = \sum_{n=1}^{10^4} d_v = \frac{w_c}{\bar{\mu}} \sum_{n=1}^{10^4} \Delta E \\ w_c = \frac{V \bar{\mu}}{E_d} \end{cases} \quad (24)$$

The friction energy dissipation per wear cycle and wear coefficient under each wear condition are shown in Fig. 14. As the tube sliding velocity or cylinder impact speed increased, the dissipated friction energy in each wear cycle increased. The wear coefficient decreased as the sliding velocity increased, whereas it increased with the impact velocity.

When the cylinder's impact velocity was reduced to zero, the normal impact force was maximized, and the pressure distribution in the contact area is

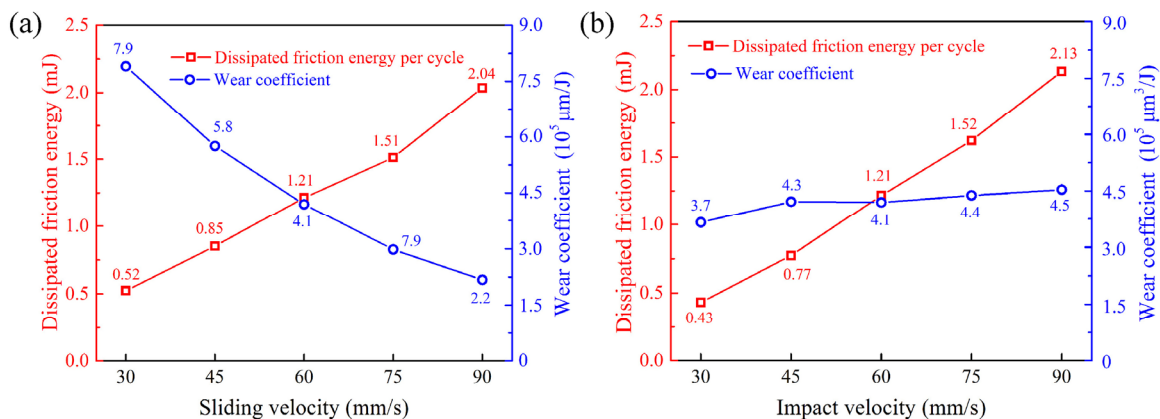


Fig. 14 Dissipated friction energy for each cycle and wear coefficient: (a) $v_i = 60$ mm/s; (b) $v_s = 60$ mm/s.

expressed as shown in Eq. (25). Based on the values estimated through a preliminary finite element analysis, the mathematical relationship between the maximum impact force and compressive stress is as shown in Eq. (26) [38]. The maximum compressive stress is proportional to the maximum impact force and inversely proportional to the wear contact area.

$$p(x, y) = p_{\text{imax}} \sqrt{1 - \frac{(x-a)^2}{a^2} - \frac{(y-b)^2}{b^2}} \quad (25)$$

$$p_{\text{imax}} \approx \frac{F_{\text{imax}}}{0.0256ab} \quad (26)$$

The followings were assumed for the semi-analytical simulations presented herein: The friction coefficient in each test was assumed to be constant and equal to the average friction coefficient. In each simulation test, the normal load and local sliding amplitude were assumed to be constant during the wear cycles. Every impact-sliding wear cycle was equally partitioned into k increments, and the tube's sliding displacement increment was d_s .

Based on the modified Archard equation expressed by Eq. (27), the wear depth increment at the point of maximum impact force was determined using Eq. (28). Additionally, because the wear amount in a single cycle must be low, we assumed that the maximum contact pressure was constant during every Δn wear cycle. Hence, the cumulative wear depth of the tube during the next Δn wear cycles can be calculated using Eq. (29). The calculations were terminated when the number of wear cycles exceeded the set maximum number of wear cycles [34, 35].

$$d_h = \frac{d_v}{d_A} = w_c \frac{F_i(t)}{d_A} d_s \quad (27)$$

$$\begin{cases} d_{h\text{max}} = w_c p_{\text{imax}} d_s \\ d_s = v_s \Delta t \\ \Delta t = \frac{2t_c}{k-1} \end{cases} \quad (28)$$

$$\Delta h_{\text{max}} = \Delta n \times d_{h\text{max}} \quad (29)$$

The evolution of the contact pressure curves along the y -axis at the point where the cylinder's impact velocity was reduced to zero is shown in Figs. 15(a)

and 15(b). As the impact-sliding wear progressed, the peaks of all the contact pressures decreased. Additionally, two small local peaks appeared at both edges of the contact region, possibly owing to the sharp profiles at the edges of the wear region and the discontinuity of the curvature radius at the borders between the worn and unworn regions, both of which can result in local stress concentrations [35, 44]. Figures 15(c) and 15(d) show the semi-analytical predicted changes in the maximum contact pressure vs. the number of wear cycles under various test conditions. All the values decreased as the number of wear cycles increased owing to the increasing contact area caused by the wear between the tube and cylinder. The reduction rate of the contact pressure decreased gradually and finally stabilized.

The maximum wear depth vs. the number of cycles under different impact-sliding wear conditions is shown in Fig. 16. The maximum wear depth increased with the tube sliding velocity or cylinder impact velocity, whereas it decreased as the number of wear cycles increased, indicating that the wear process stabilized gradually.

The wear contact area per cycle in each impact-sliding wear test can be calculated using Eq. (30) [38]. Figure 17(a) shows the size of the contact area affected by different sliding velocities at a certain impact speed. The changes in the wear contact area at various impact velocities when the sliding velocity of the tube was 60 mm/s are shown in Fig. 17(b). The results indicate that the magnitude of the increase in the contact area caused by the impact velocity was higher than that caused by the sliding velocity. The area expanded by approximately 0.065 mm² as the sliding velocity increased from 30 to 90 mm/s, whereas the area increased by approximately 0.887 mm² as the impact velocity increased from 30 to 90 mm/s at a sliding velocity of 60 mm/s.

$$A \approx \pi a(b + v_s t_c) \quad (30)$$

It is noteworthy that the results presented above were calculated values. However, in the actual wear test, owing to changes in the contact surface morphology, wear particle generation, and other factors, the maximum impact displacement of the cylinder

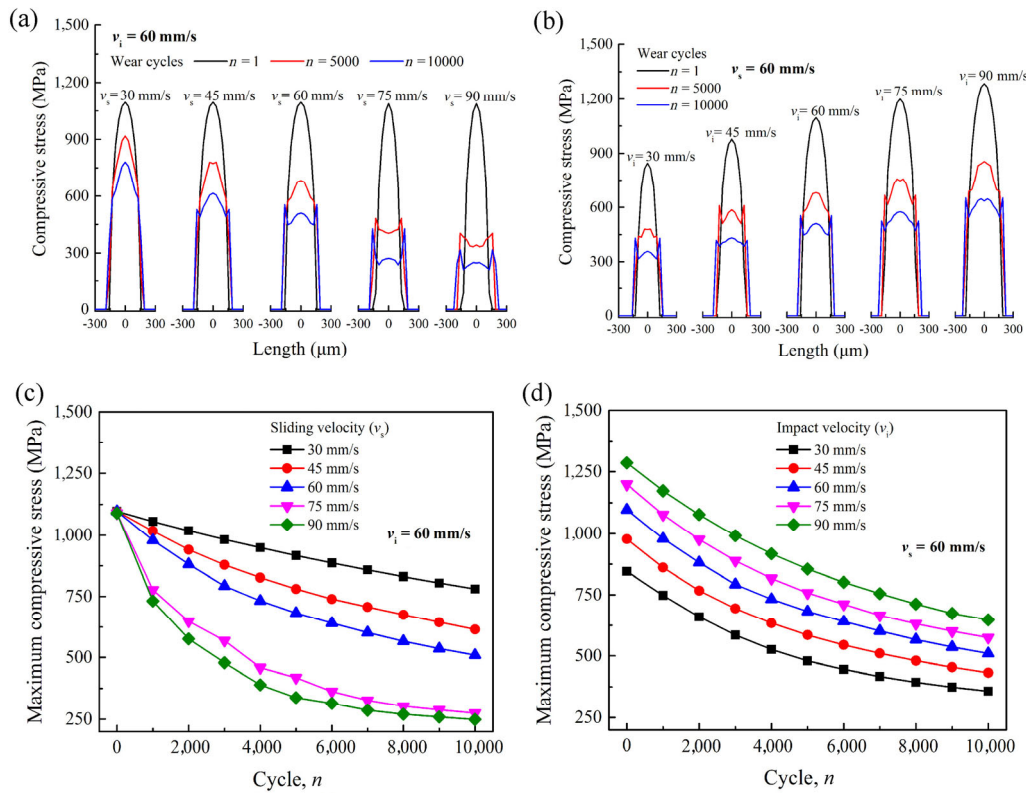


Fig. 15 Changes in maximum compressive stress vs. number of cycles: (a) contact pressure curves, $v_i = 60$ mm/s; (b) contact pressure curves, $v_s = 60$ mm/s; (c) maximum compressive stress vs. v_s ; (d) maximum compressive stress vs. v_i .

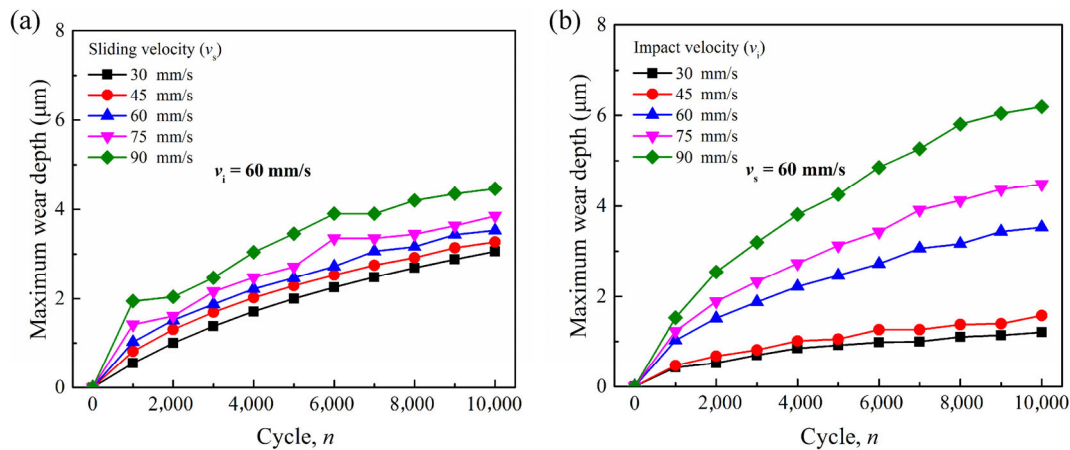


Fig. 16 Maximum wear depth vs. number of cycles: (a) maximum wear depth vs. cycles, $v_i = 60$ mm/s; (b) maximum wear depth vs. cycles, $v_s = 60$ mm/s.

changed constantly during the wear cycles. The length and width of the contact area increased with the number of wear cycles. Figure 17(c) shows the worn surfaces after 10^4 cycles of the impact-sliding simulation wear tests. As shown, all the scars were elliptical. The size of the wear surface increased with the impact or sliding velocity.

Figure 18 shows the 3D profile micrographs and

global views of the wear scars. Sliding marks were visible on the wear surfaces. The maximum wear depth appeared around the center of the sliding direction. Notable detachments were observed on all the worn surfaces, indicating abrasive wear and delamination. Additionally, debris was observed in the wear area, although most of them were on the edge of the wear scar.

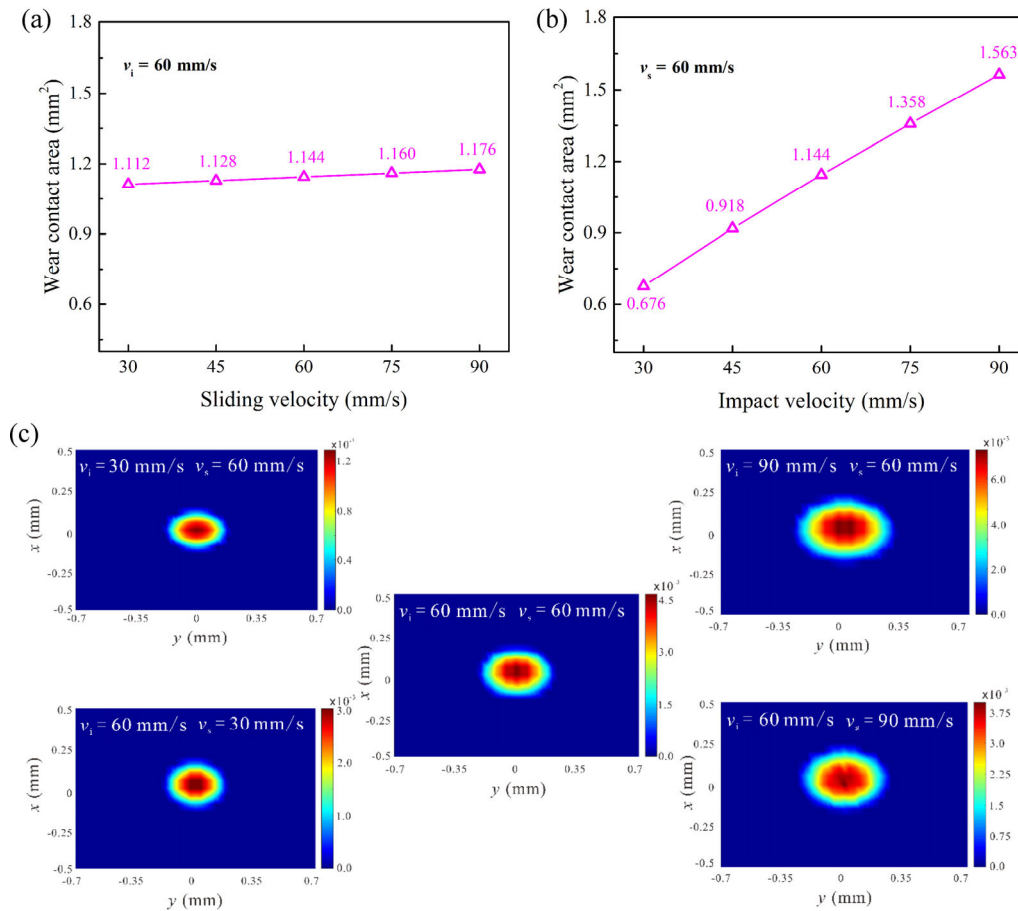


Fig. 17 Wear area under different wear conditions: (a) contact area vs. v_s , $v_i = 60$ mm/s; (b) contact area vs. v_i , $v_s = 60$ mm/s; (c) simulated wear scars, $n = 10^4$.

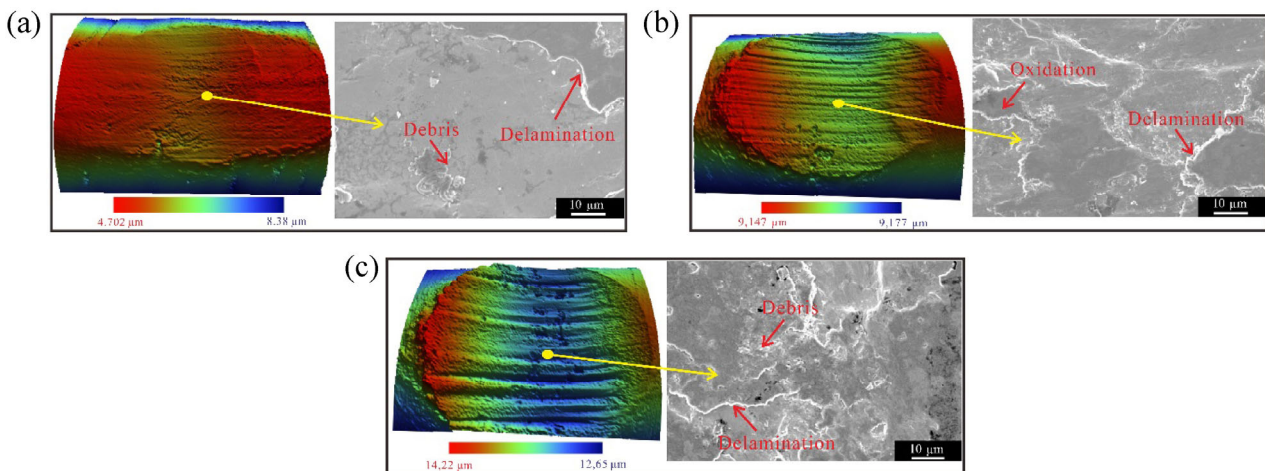


Fig. 18 Micrographs of wear scars under different wear conditions, $n = 10^4$. (a) $v_i = 30$ mm/s, $v_s = 60$ mm/s; (b) $v_i = 60$ mm/s, $v_s = 60$ mm/s; (c) $v_i = 90$ mm/s, $v_s = 60$ mm/s.

4 Conclusions

The effects of different impact and sliding velocities on the impact-sliding wear behavior were investigated

experimentally and numerically. The following conclusions are obtained:

- 1) During the impact-sliding wear process, an increase in the impact velocity increased the normal

impact force and displacement; however, changing the sliding velocity did not significantly affect these two values. The friction force increased with the impact and sliding velocities.

2) As the number of wear cycles increased continuously, the maximum impact force under each impact-sliding wear condition remained unchanged, whereas the maximum friction force first increased and then maintained a steady fluctuation in a small range.

3) The friction energy dissipated during each wear cycle increased with the sliding or impact velocity, thereby intensifying the wear of the sample tube. The wear coefficient decreased as the impact or sliding velocity increased.

4) As the impact-sliding wear progressed, the maximum wear depth increased continuously. The rate of increase decreased gradually and then stabilized. It was discovered that abrasive wear and delamination were the main wear mechanisms for this type of material.

Acknowledgements

This study is supported by the National Natural Science Foundation of China (No. U1530136) and Young Scientific Innovation Team of Science and Technology of Sichuan (No. 2017TD0017). The author Meigui YIN acknowledges the financial support from the China Scholarship Council (CSC No. 201907000021).

Open Access This article is licensed under a Creative Commons Attribution 4.0 International License, which permits use, sharing, adaptation, distribution and reproduction in any medium or format, as long as you give appropriate credit to the original author(s) and the source, provide a link to the Creative Commons licence, and indicate if changes were made.

The images or other third party material in this article are included in the article's Creative Commons licence, unless indicated otherwise in a credit line to the material. If material is not included in the article's Creative Commons licence and your intended use is not permitted by statutory regulation or exceeds the permitted use, you will need to obtain permission directly from the copyright holder.

To view a copy of this licence, visit <http://creativecommons.org/licenses/by/4.0/>.

References

- [1] Lyerly R L. *Nuclear Power Plants*. US Atomic Energy Commission: Division of Technical Information, 1967.
- [2] Murty K L, Charit I. Structural materials for Gen-IV nuclear reactors: Challenges and opportunities. *J Nucl Mater* **383**(1–2): 189–195 (2008)
- [3] Locatelli G, Mancini M, Todeschini N. Generation IV nuclear reactors: Current status and future prospects. *Energy Policy* **61**: 1503–1520 (2013)
- [4] Cai Z B, Li Z Y, Yin M G, Zhu M H, Zhou Z R. A review of fretting study on nuclear power equipment. *Tribol Int* **144**: 106095 (2020)
- [5] Lai P, Gao X C, Tang L C, Guo X L, Zhang L F. Effect of temperature on fretting wear behavior and mechanism of Alloy 690 in water. *Nucl Eng Des* **327**: 51–60 (2018)
- [6] Wang W, Li C, Shang S L, Cao J Z, Liu Z K, Fang C. Study on impact of Cr and Mo on diffusion of H in 2.25Cr–1Mo steel using first-principle calculations. *J Nucl Mater* **525**: 152–160 (2019)
- [7] Zhang X Y. Studies on tangential fretting wear mechanisms of steam generator tubes in nuclear power systems. Ph.D. Thesis. Chengdu (China): Southwest Jiaotong University, 2013.
- [8] Guo X L, Lai P, Li L, Tang L C, Zhang L F. Progress in studying the fretting wear/corrosion of nuclear steam generator tubes. *Ann Nucl Energy* **144**: 107556 (2020)
- [9] Soria S R, Tolley A, Yawny A. A study of debris and wear damage resulting from fretting of Incoloy 800 steam generator tubes against AISI Type 304 stainless steel. *Wear* **368–369**: 219–229 (2016)
- [10] Zhang B B, Wang J Z, Yuan J Y, Yan F Y. Tribocorrosion behavior of nickel-aluminium bronze sliding against alumina under the lubrication by seawater with different halide concentrations. *Friction* **7**(5): 444–456 (2019)
- [11] Meng Y G, Xu J, Jin Z M, Prakash B, Hu Y Z. A review of recent advances in tribology. *Friction* **8**(2): 221–300 (2020)
- [12] Abbas T, Khushnood S, Nizam L, Usman M. Fretting wear analysis of different tube materials used in heat exchanger tube bundle. *Adv Sci Technol Res J* **11**(4): 123–133 (2017)
- [13] Guo X L, Lai P, Tang L C, Chen K, Zhang L F. Time-dependent wear behavior of Alloy 690 tubes fretted against 405 stainless steel in high-temperature argon and water. *Wear* **414–415**: 194–201 (2018)

- [14] Souilliar T, Rigaud E, Le Bot A, Phalippou C. An energy approach for impact wear in water environment. *Wear* **376–377**: 738–746 (2017)
- [15] Souilliar T, Rigaud E, Le Bot A, Phalippou C. Energy-based wear law for oblique impacts in dry environment. *Tribol Int* **105**: 241–249 (2017)
- [16] Cai Z B, Guan H D, Chen Z Q, Qian H, Tang L C, Zhou Z R, Zhu M H. Impact fretting wear behavior of 304 stainless steel thin-walled tubes under low-velocity. *Tribol Int* **105**: 219–228 (2017)
- [17] Guan H D, Cai Z B, Ren Y P, Jing J Y, Wang W J, Zhu M H. Impact-fretting wear behavior of Inconel 690 alloy tubes effected by pre-compressive stress. *J Alloys Compd* **724**: 910–920 (2017)
- [18] Sun Y, Cai Z B, Chen Z Q, Qian H, Tang L C, Xie Y C, Zhou Z R, Zhu M H. Impact fretting wear of Inconel 690 tube with different supporting structure under cycling low kinetic energy. *Wear* **376–377**: 625–633 (2017)
- [19] Guo K, Jiang N B, Qi H H, Feng Z P, Wang Y, Tan W. Experimental investigation of impact-sliding interaction and fretting wear between tubes and anti-vibration bars in steam generators. *Nucl Eng Technol* **52**(6): 1304–1317 (2020)
- [20] Van Herpen A, Reynier B, Phalippou C. Effect of test duration on impact/sliding wear damage of 304L stainless steel at room temperature: Metallurgical and micromechanical investigations. *Wear* **249**(1–2): 37–49 (2001)
- [21] Chen Z Q. Development of the impact-sliding wear test rig and experimental research, M.S. Thesis. Chengdu (China): Southwest Jiaotong University, 2017.
- [22] Yin M G, Cai Z B, Yu Y Q, Zhu M H. Impact-sliding wear behaviors of 304SS influenced by different impact kinetic energy and sliding velocity. *Tribol Int* **143**: 106057 (2020)
- [23] Yin M G, Cai Z B, Zhang Z X, Yue W. Effect of ultrasonic surface rolling process on impact-sliding wear behavior of the 690 alloy. *Tribol Int* **147**: 105600 (2020)
- [24] Guo X L, Lai P, Tang L C, Wang J M, Zhang L F. Effects of sliding amplitude and normal load on the fretting wear behavior of Alloy 690 tube exposed to high temperature water. *Tribol Int* **116**: 155–163 (2017)
- [25] Mi X, Wang W X, Xiong X M, Qian H, Tang L C, Xie Y C, Peng J F, Cai Z B, Zhu M H. Investigation of fretting wear behavior of Inconel 690 alloy in tube/plate contact configuration. *Wear* **328–329**: 582–590 (2015)
- [26] Xin L. Fretting wear behavior and damage mechanism of nuclear grade Inconel 690TT alloy. Ph.D. Thesis. Beijing (China): University of Science and Technology Beijing, 2018.
- [27] Xin L, Yang B B, Wang Z H, Li J, Lu Y H, Shoji T. Effect of normal force on fretting wear behavior and mechanism of Alloy 690TT in high temperature water. *Wear* **368**: 210–218 (2016)
- [28] Guan H D. Study on the impact fretting wear behavior of 304 stainless steel and 690 alloy thin wall tubes. M.S. Thesis. Chengdu (China): Southwest Jiaotong University, 2018.
- [29] Sato Y, Iwabuchi A, Uchidate M, Yashiro H. Dynamic corrosion properties of impact-fretting wear in high-temperature pure water. *Wear* **330–331**: 182–192 (2015)
- [30] Attia H. A Generalized Fretting Wear Theory. *Tribol Int* **42**(9): 1380–1388 (2009)
- [31] Renouf M, Massi F, Fillot N, Saulot A. Numerical tribology of a dry contact. *Tribol Int* **44**(7–8): 834–844 (2011)
- [32] Beyer T, Chaise T, Leroux J, Nélías D. A damage model for fretting contact between a sphere and a half space using semi-analytical method. *Int J Solids Struct* **164**: 66–83 (2019)
- [33] Chaise T, Nélías D, Sadeghi F. On the effect of isotropic hardening on the coefficient of restitution for single or repeated impacts using a semi-analytical method. *Tribol Trans* **54**(5): 714–722 (2011)
- [34] Gallego L, Nélías D, Jacq C. A comprehensive method to predict wear and to define the optimum geometry of fretting surfaces. *J Tribol* **128**(3): 476–485 (2006)
- [35] Chen Y, Meng F. Numerical study on wear evolution and mechanical behavior of steel wires based on semi-analytical method. *Int J Mech Sci* **148**: 684–697 (2018)
- [36] Stronge W J. *Impact Mechanics*. Cambridge (UK): Cambridge University Press, 2018.
- [37] Engel P A, Ling F F. Impact wear of materials. *J Appl Mech* **45**(2): 458–459 (1978)
- [38] Johnson K L. *Contact Mechanics*. Cambridge (UK): Cambridge University Press, 1987.
- [39] Mindlin R D, Deresiewicz H. Elastic spheres in contact under varying oblique forces. *J Appl Mech* **20**(3): 327–344 (1953)
- [40] Persson B N J, Tosatti E. *Physics of Sliding Friction*. Dordrecht: Springer the Netherlands, Dordrecht Press, 1996.
- [41] Popov V L. *Contact mechanics and friction*. Berlin (Germany): Springer Berlin Heidelberg, 2010.
- [42] Fouvry S, Liskiewicz T, Kapsa P, Hannel S, Sauger E. An energy description of wear mechanisms and its applications to oscillating sliding contacts. *Wear* **255**(1–6): 287–298 (2003)
- [43] Hegadekatte V, Kurzenhäuser S, Huber N, Kraft O. A predictive modeling scheme for wear in tribometers. *Tribol Int* **41**(11): 1020–1031 (2008)
- [44] Mattei L, di Puccio F. Influence of the wear partition factor on wear evolution modelling of sliding surfaces. *Int J Mech Sci* **99**: 72–88 (2015)



Meigui YIN. He received his Ph.D. degree in mechanical engineering in 2020 from the Institute of Tribology at Southwest Jiaotong

University. His research interests include impact-sliding wear behaviors of different nuclear materials and tribology equipment development.



Chaise THIBAUT. He is an assistant professor of mechanical engineering at the LaMCoS laboratory, INSA Lyon. His research deals with contact mechanics, material behaviours

characterization and modelling at high temperature, thermal rate and strain rate, and the modelling and development of processes (welding, peening, and additive manufacturing).



Liwen WANG. He received his Ph.D. degree in mechanical engineering from Harbin Institute of Technology, Harbin, China, in 2011. He currently serves as the director

level researcher in the Academia Sinica of Dongfang Electric Co., Ltd. His research interests are vibration monitoring and fault diagnosis, and flow-induced vibration test technology of nuclear power equipment.



Daniel NÉLIAS. He received his Ph.D. degree in mechanical engineering from INSA Lyon, France, in 1989. His current position is a

professor and the director of the LaMCoS laboratory. His research deals with contact mechanics and the modelling of fretting wear under various service conditions.



Minhao ZHU. He received his M.S. and Ph.D. degrees in metal material and heat treatment from Southwest Jiaotong University, Chengdu, China, in 1993 and 2001, respectively. He

joined the Institute of Tribology at Southwest Jiaotong University in 1997. His current position is a professor. His research areas cover the engineering materials for tribological surfaces.



Zhenbing CAI. He received his Ph.D. degree in materials science from Southwest Jiaotong University, China, in 2009. He joined the Mechanical Engineering School at Southwest Jiaotong University in

2009. His current position is a professor and the director of the Tribology Research Institute. His research areas cover the wear damages of steam generator tubes for nuclear power plants and the engineering materials for tribological surfaces.